Effect of abrasive water jet peening on NaCl-induced hot corrosion behavior of Ti-6Al-4V

V. Chakkravarthy [a,*], J.P. Oliveira [b,**], Anisa Mahomed [c], Nan Yu [d], P. Manojkumar [e],

M. Lakshmanan [f], Long Zhang [g], V. Raja [h], S. Jerome [e], T. Ram Prabhu [i], R.L. Narayan [j,***]

[a] Department of Metallurgical and Materials Engineering, Indian Institute of Technology Madras,

Chennai, Tamilnadu, India

[b] CENIMAT/I3N, Department of Materials Science, NOVA School of Science and Technology,

Universidade NOVA de Lisboa, Caparica 2829-516, Portugal

[c] Chemical Engineering and Applied Chemistry, School of Infrastructure and Sustainable

Engineering, College of Engineering and Applied Science, Aston University, Birmingham, B4

7ET, UK

[d] Institute of Materials and Processes, School of Engineering, University of Edinburgh, EH9

3FB, Scotland, UK

[e] Department of Metallurgical and Materials Engineering, National Institute of Technology,

Tiruchirappalli, Tamilnadu, India

[f] Department of Mechanical Engineering, Ramco Institute of Technology, Rajapalayam,

Tamilnadu, India

[g] Institute of Metal Research, Chinese Academy of Sciences, Shenyang, 110016, China

[h] Department of Production Engineering, PSG College of Technology, Coimbatore, Tamilnadu,

India

[i] CEMILAC, Defense R&D Organization, Bangalore, 560037, India

[j] Department of Materials Science and Engineering, Indian Institute of Technology Delhi, Hauz

Khas, New Delhi, 110016, India

*Corresponding authors: chakkravarthyv5@gmail.com, jp.oliveira@fct.unl.pt,

rlnarayan@iitd.ac.in

Abstract

Hot corrosion studies were performed on pristine and abrasive water jet peened (AWJP) Ti–6Al–4V surfaces. Oxide scales form on the peened and pristine surfaces when coated with NaCl and exposed to 600 °C for 100 h. Despite similar oxide compositions on both surfaces, the thickness and roughness of the oxide scale on the AWJ peened surface is lower. The hot corrosion rate of the pristine surface is 2.5 times higher than that on the AWJ peened surface. Enhanced hot corrosion resistance of the latter is attributed to compressive residual stresses on the surface that retards diffusion of chloride in the material.

1. Introduction

Ti–6Al–4V alloy is widely used in the fabrication of gas turbine engine components and fuel storage tanks of jet engines [1,2,3] due to its high specific strength and excellent elevated temperature mechanical properties [4,5]. Additionally, they have good corrosion resistance in ambient conditions as a stable and coherent TiO2 film, which prevents its further oxidation, forms on the surface. However, when exposed to corrosive environments at high temperatures, components made from Ti–6Al–4V undergo hot corrosion. Hot corrosion occurs when a metallic component is repeatedly exposed to extremely high temperatures in the presence of difficult

service environments like alkali sulphate deposits or sulfur-containing gases [[6], [7], [8]]. For instance, some of the by-products that get generated from the combustion of low-grade oil fuels such as, Na2SO4, NaCl and V2O5, are highly corrosive [9]. Of these, NaCl causes the most intense hot corrosion damage in Ti–6Al–4V [10]. Prolonged exposure of the component to NaCl at temperatures ≥ 600 °C leads to the formation of a dense oxide scale over the alloy surfaces. Anuwar et al. [11] also noted that low altitude flying aircraft components made from Ti–6Al–4V experiences hot corrosion attack while flying across the sea, which is abundant in NaCl. It the context of preventive measures for hot corrosion, it was observed that several surface modification techniques such as Hot Isostatic Pressing (HIPing) [12], laser shock peening [13,14], surface coating [15], shot peening [16], ultrasonic peening [9] and electrochemical processing [17] help in mitigating hot corrosion damage caused by NaCl. The subsurface modification depth in these techniques can range from few μm to mm [18]. For instance, Kumar et al. showed that ultrasonic shot peening of Ti–6Al–4V can modify the material microstructure to a maximum depth ~ 30 μm [19]. Alternately, Guo et al. demonstrated that laser shock peening can effectively modify the material up to a depth of 900 μm [14] whereas Childerhouse et al. assessed that (HIPing) can modify the surface of Ti–6Al–4V up to a depth of 500 μm [20]. Considering that hot corrosion attack in Ti–6Al–4V generally occurs in subsurface layers that are at a depth of 10–30 μm only, some of these surface modification methods can be considered decadent [21]. It is therefore necessary to identify a low-cost surface modification technique that can achieve the appropriate degree of surface modification in the material that is necessary to prevent corrosion. In that context, Natarajan et al. pointed out that abrasive water jet (AWJ) peening, a relatively inexpensive surface modification technique, can introduce compressive residual stresses up to a depth of 50 μm [22].

A similar depth of surface modification was also observed when AWJ peening was performed on Inconel 718.

AWJ peening uses a high-pressure water jet and a hard abrasive, such as garnet or crushed alumina, to create a hammering effect over the surface. During AWJ peening, abrasives bombard the workpiece with a very high kinetic energy and refine the grain structure up to a depth of ~40 μm. Compressive residual stresses develop in the material, which significantly improves its hardness [23]. However, only an optimum degree of AWJ peening is desired as prolonged exposure can damage the surfaces and produce stress raisers, which deteriorates fatigue life significantly [24]. Liao et al. and Amar et al. reported that the use of sharp abrasive particles intensifies the surface damage during multipass water jet peening [23,25].

To attenuate surface damage during AWJ processing, Liao et al. developed a novel idea of using soft and blunt abrasive particles as the peening media [23]. In addition, their work provided a guideline to optimize synergistic process parameters such as water pump pressure, jet feed speed, kerf profile, inclination angle of the jet plume and critical Standoff Distance (SoD) to ensure the appropriate level of subsurface modification, without compromising surface integrity.

While studies on the improvement of hot corrosion resistance of ultrasonic shot peened and laser shock peened Ti–6Al–4V surfaces are available in the literature [9,13], that of AWJ peening is underrepresented.

Motivated with the intention of filling this knowledge gap, the present study investigates the effect of AWJ peening on the hot corrosion resistance of Ti–6Al–4V. For this, the microstructures, residual stress profiles and surface roughness profiles of pristine and AWJ peened Ti–6Al–4V surfaces are compared. Both surfaces are coated with NaCl and exposed to a temperature of 600 °C for 100 h. Post facto compositional and morphological examination of the corroded surfaces are performed to understand the nature of passive films and scales formed on the surface. Based on the results, the chemistry, corrosion kinetics and hot corrosion mechanisms of the AWJ peened and pristine Ti–6Al–4V are discussed in detail. Finally, the role played by atmospheric oxygen and the surface modification on hot corrosion resistance of the alloy is summarized.

2. Experimental procedures

2.1 Materials

The workpiece material employed in this study was α + β alloy ASTM B265 Ti-6Al-4V Grade 5 whose nominal chemical composition is shown in Table-1. Using wire cut electric-discharge machining (W-EDM) the plate was cut into smaller specimens of dimensions 100mm × 100mm × 5mm. The surface of the as-received workpiece had already been processed, and hence did not require further finishing.

Table 1. Chemical combination of Ti-6Al-4V alloy.

Element	Titanium	Aluminum	Vanadium	Iron	Carbon	Nitrogen	Oxygen
Content (wt. %)	87.6–91	6.75	4.5	≤0.40	≤0.080	≤0.050	≤0.20

2.2 Abrasive water jet machining experimental setup

The experimental setup of the AWJ processing is shown in Fig. 1. Surface modifications were carried out using an OMAX MAXIEM AWJ machine (Model:1515) on one side of the work piece whereas the other side was left in the as received state. The two surfaces will be referred to as AWJ peened and pristine surfaces respectively. It was previously shown that for surface peening, blunt and soft abrasives are preferred over sharp ones. Therefore, to avoid metal removal while peening, a blunt alumina abrasive of less than #80 mesh size was chosen in this study. For smooth flow of abrasives and to avoid clogging of the nozzle, the machine manufacturer (OMAX-MAXIEM) recommends the use of abrasives with a mesh size less than #80. The impact angle (i.e. the jet impingement angle) was kept at 30° to attenuate the kinetic energy of the abrasive particles, which in turn, would prevent erosion of the surface and reduces the crater depth. Optimal process parameters were selected based on pilot experiments and previous research work [22,23]. The considered optimal process parameters are listed in Table-2.
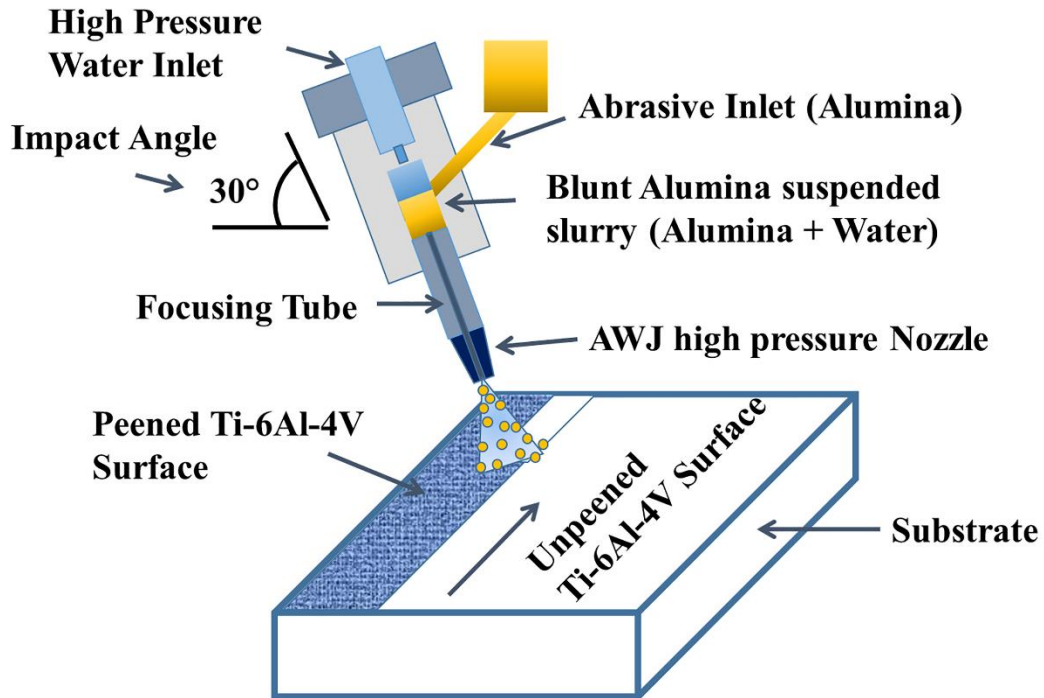
Fig.1. Schematic illustration of Abrasive Water Jet peening of Ti-6Al-4V

Table 2. Optimal AWJ peening process parameters

Technical considerations for AWJ Peening process	Input
Orifice nozzle diameter [mm]	1.9
Pump pressure [MPa]	120
Impact angle [º]	30
Traverse speed [mms−1]	7.5
Stand-off distance [mm]	40
Focusing tube diameter (mm)	0.9
Abrasive mass flow rate (l/min)	12
Processing time (s/mm)	10
Abrasive material (Crushed Al_2O_3 balls) µm	80

2.3 Residual stress analysis

The residual stress distribution along the cross section of the AWJ peened and pristine surfaces were measured by an X-ray Diffractometer (Proto-XRD, Canada) with the $\sin^2(\psi)$ method. Cu-Kα radiation (λ = 1.541838 Å) with a Nickel filter was used as the X-ray source. The voltage, current and X-ray beam diameter were set as 30 kV, 25 mA and 1 mm respectively. In the present study, the X-ray was diffracted in {213} α-Ti diffraction plane at different title angles (Ψ) angles 0°, 25°, 35° and 45°. To obtain the residual stress across the depth of the processed material, thin layers of the surface were successively removed by electrolytic polishing. Later, residual stresses were measured in 13 equidistant points along the cross-sectional depth of scan area approximately (25mm×25mm).

2.4 Hot corrosion testing

For comparison, AWJ peened and unpeened samples were subjected to hot corrosion testing. NaCl is one of the most common salts that causes corrosion at elevated temperatures, both samples were exposed to 100% NaCl using a spray gun. Samples were then baked to remove existing moisture. Prior to hot corrosion testing, samples were weighed after coating with NaCl. The salt concentration over the surfaces was found to be 50−55 mg/cm^2. The dried samples were kept in an electrical resistance furnace at a temperature of 600°C for a period of 100 hours which was sufficient to generate representative corrosion damage. The series of steps involved in hot corrosion analysis is shown in Fig.2.
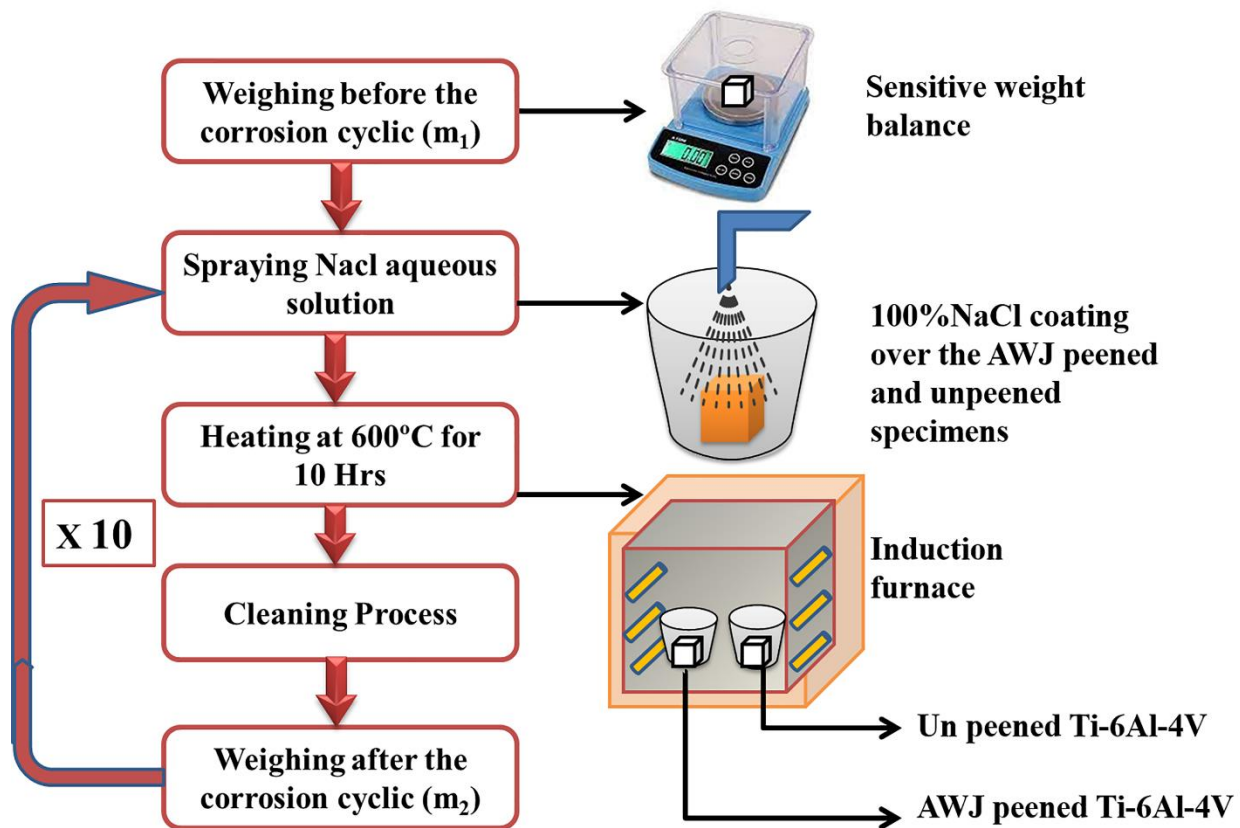

Fig.2. Schematic illustration of steps involved in hot corrosion analysis.

2.5. Surface morphology

The machined surface morphology and corroded morphologies were captured using Scanning Electron Microscopy (SEM) (Model: Zeiss EV18) and Energy Dispersive Spectroscopy (EDS) (Model: a Bruker X-Flash). Grain orientation maps were generated using EBSD to analyze the impact of strain hardening behavior (Model: Fei Quanta 200 HV). The surface topology of the machined surface was captured using an Atomic Force Microscope (AFM), (Model: NTEGRA Prima). Furthermore, the passive film chemistry was probed via X-ray Photon Spectroscopy (XPS) (Model: AXIS Supra+) with an Al Kα as an excitation source (hv = 1486.6 eV). The base pressure of the ultra-high vacuum system was at the level of 10^{-8} Pa. All spectra were collected from the electron emission angle set at 90∘, and an area with a diameter of 500 μm analyzed. The high-resolution spectra were recorded with the pass energy at 30 eV. Samples were not sputter-etched before analyses. Also, no charge neutralizer was utilized during the investigation. The spectra were fitted using the CasaXPS using a mixed Gaussian-Lorentzian fitting model. All spectra have been referenced to the binding energy (B.E) of the C 1s peak. This traditional calibration with C 1s Peak of Adventitious carbon promotes high risk and leads to non-physical results [26–28]. To avoid such irregularity in the XPS results, the C 1s binding energy was calibrated using Eq. (1a)

$$\textbf{\textit{EFB}+}\boldsymbol{\varphi}\textbf{\textit{SA}} = \textbf{289.58 \textit{eV}} \tag{1a}$$

where *EFB* and *φSA* are the binding energies of the C 1s peaks of indefinite carbon, referenced to the Fermi edge and work function of TiO2, respectively. The work function of TiO2 is set to be 4.90 eV as reported in literature [29,30]. Then the *EFB* of the C 1s peak is calculated to be 284.68 eV and this value of C 1s peak is used to calibrate the entire XPS spectra. Also, the sample was not sputter-etched in order to preserve the surface status prior to XPS measurement. Furthermore, to corroborate with the oxide scale chemistry, transmission electron microscopy (TEM) was performed for hot corroded AWJP specimens using JEOL (JEM-2100) TEM.
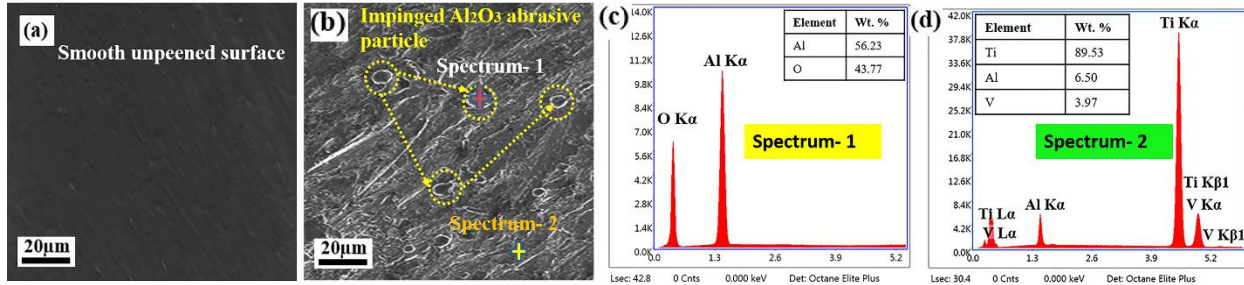
3. Results

Fig.3 (a) Surface morphology of pristine Ti-6Al-4V surface, (b) Surface morphology of AWJ peened Ti-6Al-4V surface, (c) EDS point mapping of impinged abrasive particle, (d) EDS point mapping of workpiece surface.

3.1. Microstructural evolution in pristine and AWJ peened Ti-6Al-4V surfaces

Fig.3(a) and 3(b) show the smooth surface morphology of the pristine Ti-6Al-4V surface the AWJ peened surface. Traces of the impinged (Al_2O_3) abrasive balls are observed on the workpiece, which is also confirmed from the EDS maps shown in Fig. 3(c) (labelled as spectrum-1). Results of the EDS point mapping of other areas on the AWJ peened surface, marked as spectrum-2 and shown in Fig. 3(d), reveals the presence of a needle like α (HCP) phase and secondary β (BCC) phase.

Fig. S1 of the Supplementary Information (SI) displays the Optical profilometer images of the pristine and AWJ peened surfaces. The AWJ peened surfaces exhibit an average surface roughness, R_a, of ~8.2± 0.02 μm, which is at least 4 times higher than that of the pristine surface. Next, the variations of the residual stresses of the pristine and AWJ peened portions as a function of the depth measured from the surface are shown in Fig. 4. While the pristine portion exhibits negligible residual stresses, the peened portion exhibits a compressive residual stress of -351 MPa ± 10 MPa at the surface. With increasing depth, the pristine portion exhibits tensile residual

10

stresses, which reaches a maximum of 100 MPa at a depth of 60 µm. The increase in tensile residual stresses in the pristine portion with increasing depth is attributed to the processing treatments that were performed on the sample prior to being supplied in the as-received condition. The magnitude of the residual compressive stresses on the peened portion gradually reduces with increasing depth and is -51 ± 10 MPa at a depth of 60 µm.
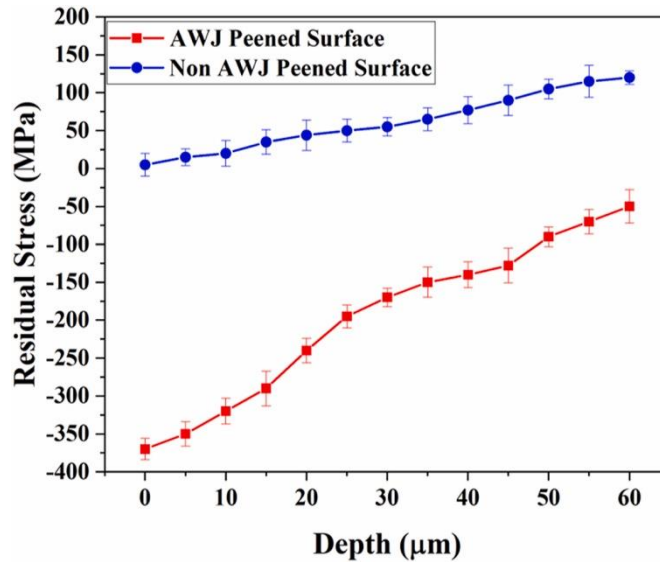

Fig.4. X-ray residual stress analysis of pristine and AWJ peened surfaces.

To understand the microstructure and phase evolution of these two surfaces, their XRD and EBSD results were analyzed. XRD patterns of pristine and AWJ peened Ti-6Al-4V surfaces are shown in Fig. 5. Peaks corresponding to α-Ti, i.e., (100), (002), (101), (102), (110), (103), (112), (201) and those of β-Ti, (110), are identified in both surfaces. Given that the majority of diffraction peaks correspond to the α-phase, it is the dominant phase in the alloy. Although no new additional peaks were observed after AWJ peening, the peaks are broadened and shifted to lower 2θ compared to that of the pristine surface. For instance, the full width at half maximum (FWHM) of α (110) peak broadens from 0.22° to 0.32°. These observations suggest that the AWJ surface has undergone

significant lattice distortion in the form of plastic deformation, which is consistent with the observations of Guo et al.[14].
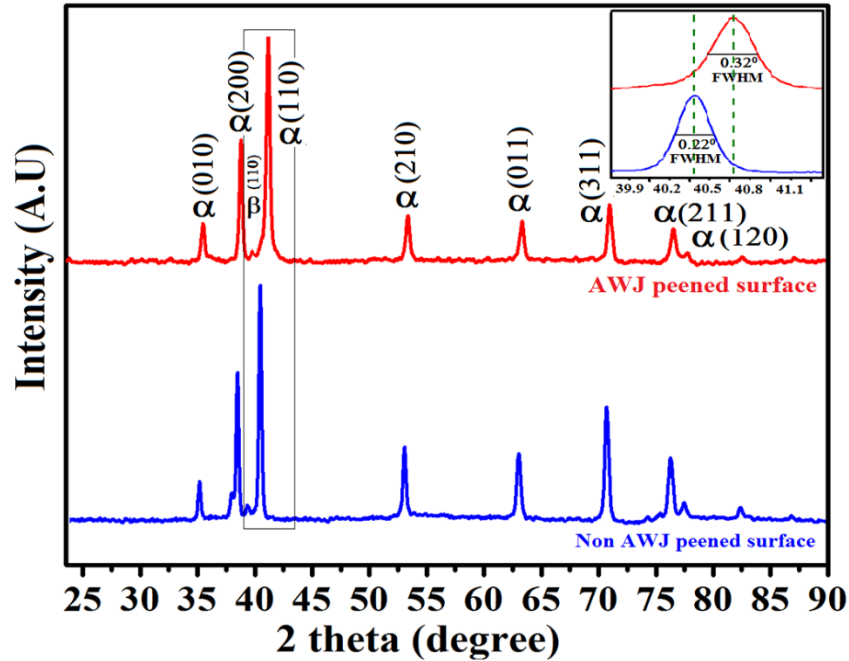

Fig.5 X-ray Diffraction pattern of pristine and AWJ peened surfaces.

The EBSD Inverse Pole (IP) figures of the pristine and AJW peened surfaces are shown in Fig. 6(a) and 6(b). While the average grain sizes are similar in the pristine and AJW peened surfaces, several small spots are visible in the latter. Kernel average misorientation mapping (KAM) of the grains in the peened surface, shown in Fig. S2 of SI, suggests that these spots have a misorientation of 0-5°, which implies that they are sub-grains. The formation of sub-grains within grains is consistent with that reported in previous studies on AWJ peening [23]. Phase mapping shown in Fig. S3 reveals that some spots also correspond to the transformed β phase, which implies that AWJ peening also results in their refinement.
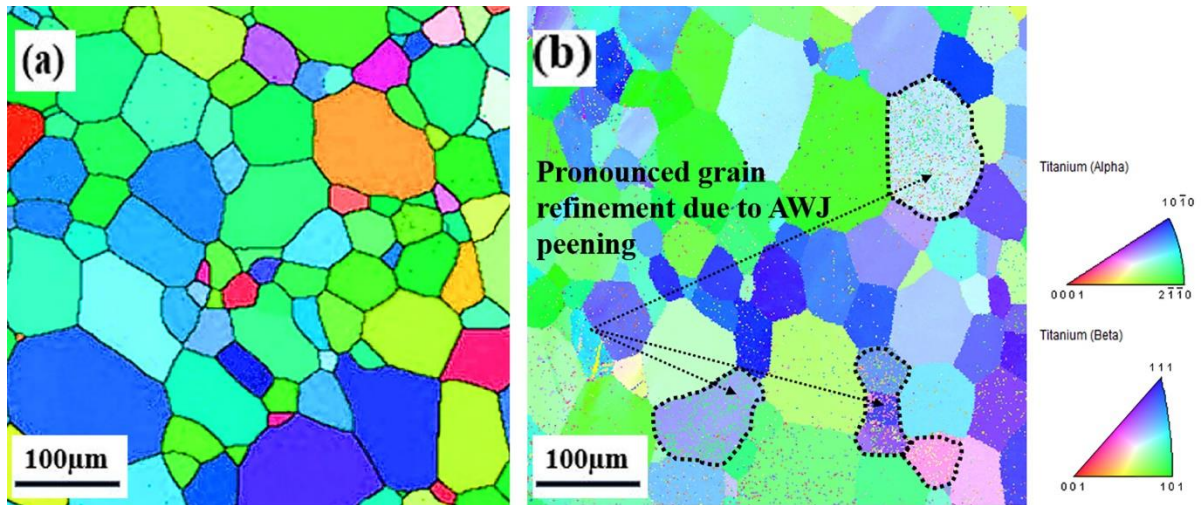
Fig.6. EBSD IP maps of (a) pristine and (b) AWJ peened Ti-6Al-4V surfaces. The IP figures are shown on the right.

To further understand the mechanical property changes due to AWJ peening, microhardness was evaluated for the peened and pristine surfaces. Fig. 7 shows the variations of hardness as a function of depth from the surface of the AWJ peened and pristine surfaces. At the surface, the AWJ peened portion and pristine portion have a hardness of 412 ±5 HV and 375 ±5 HV, respectively. The hardness of the pristine portion remains mostly invariant, barring minor fluctuation, with increasing depth, whereas that of the peened portion increases initially to 435 HV, up to a depth of 20 µm, and then decreases gradually. At a depth of 90 µm, the hardness of both the peened and pristine portions are ~387.5 HV. On average, the hardness of the AWJ peened portion is 402.1 HV, whereas that of the pristine portion is 368 HV. A similar increase in the hardness of the sub-surface layer in peened Ti-6Al-4V, up to a depth of 35µm, was observed by Liao et al. [20]. They attributed it to the presence of the β phase in the alloy, which undergoes more plastic deformation than the α phase. This leads to work hardening to greater depths in the alloy compared to that in an alloy that only contains the α phase.

13

Overall, AWJ peening increases the surface roughness and facilitates plastic deformation of Ti-6Al-4V, which in turn leads to build up of compressive residual stresses in it. The latter increases the hardness of the AWJ peened surface compared to the pristine surface. Moreover, AWJ peening also breaks up the β phase and creates several sub-grains in the alloy.
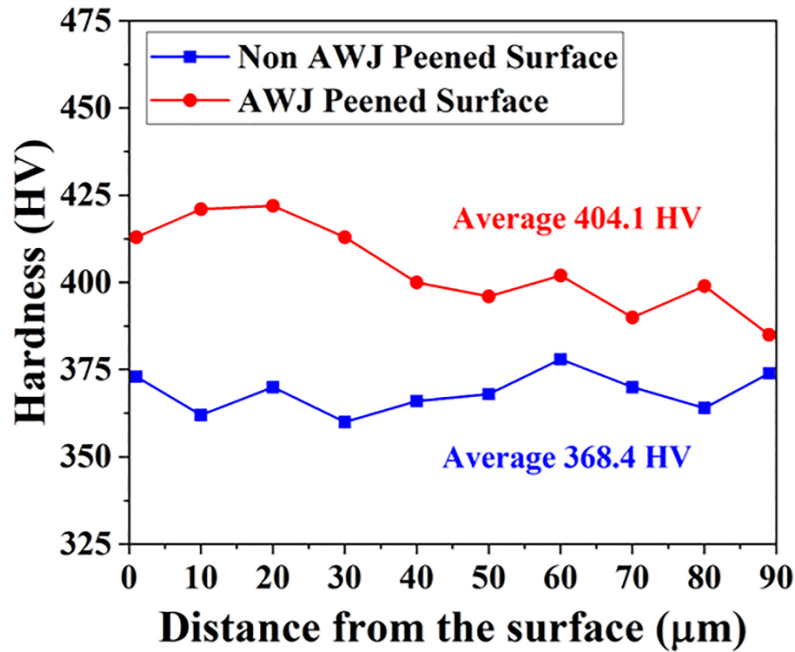

Fig.7 Variations of Hardness on the cross-section along the depth of the pristine and AWJ peened surfaces.

3.2. Hot corrosion of pristine and AWJ peened Ti-6Al-4V surfaces

The two surfaces coated with 100% NaCl and subjected to 600 °C for 100 h was examined at different time intervals. Initially, after 10 hrs, an outer scale was formed on both the surfaces. However, after 15-20 h of exposure, the outer scale on the pristine surface peeled off, facilitating the formation of an inner scale. On the other hand, the outer scale on the AWJ peened surface remained intact. Nevertheless, both surfaces contained minute pores and cracks.

Next, the oxidation and hot corrosion kinetics of the two coated surfaces was examined. The rate of oxidation is evaluated in terms of mass change per unit area, $\Delta w/A$, at different intervals of time, t. The variations of gross mass gains of the two surfaces as a function of t are presented in Fig.8a. While $\Delta w/A$ increases on both surfaces with increasing t, the rate and magnitude of the increase are different. Despite having a similar initial $\Delta w/A$ of ~0.5 mg/cm^2, the pristine Ti-6Al-4V surface gains mass at a faster rate than the AWJ peened surface. For instance, after t ~50 hrs of exposure, the AWJ peened surface and pristine surfaces exhibit $\Delta w/A$ ~1.2 mg/cm^2 and ~3 mg/cm^2, respectively. After t ~100 hrs, a further increase in $\Delta w/A$ of only 0.3 mg/cm^2 is observed on the AWJ peened surface, whereas the $\Delta w/A$ of the pristine surface increases by $\approx$ 2 mg/cm^2.

Previous studies [6,8] have shown that the variations of $\Delta w/A$ with t are well-described by the power law relation,

$$\left(\frac{\Delta w}{A}\right)^2 = K_p t + C \tag{1b}$$

where K_P is the parabolic rate constant (mg^2/cm^4/h) and C is another fitting constant. A good fit, with R^2 ~0.99, is obtained when the weight-gain plots of the pristine and AWJ peened surfaces are fitted with eq. 1, as shown in Fig. 8(b). K_P for AWJ peened and pristine surfaces are $\approx$ 0.08 mg^2/cm^4/h and 0.2 mg^2/cm^4/h, respectively. The higher K_P of the pristine surface is consistent with the observation that it gains mass at a faster rate. A similar drop in the corrosion rate was observed in ultrasonic peened and laser shock peened Ti-6Al-4V alloys compared to that in the pristine condition on coating with reactive salts [9,13].
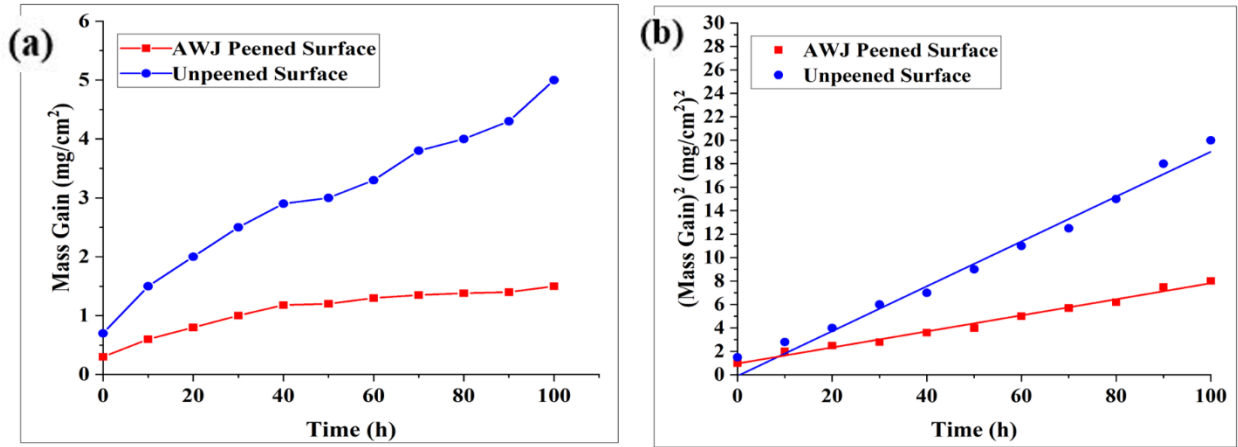
Fig.8. Variations of (a) mass gain and (b) square of weight-gain per unit area with time of pristine and AWJ peened Ti-6Al-4V surfaces during hot corrosion.

To understand the origin and variations in mass gain, the microstructures of both specimens are examined with SEM. Cross-sectional images of both AWJ peened and pristine hot corroded samples are presented in Fig.9. Apart from Ti, Al and V, the top layer of both surfaces contain oxygen, which implies that an oxide scale has formed. The thickness of the oxide scale on the AWJ peened surface is 1.5 µm and that of the pristine surface is only 4 µm. Fig. S4 displays the optical profilometer images of the hot corroded pristine and AWJ peened surfaces coated with oxides. The R_a of the oxides on the AWJ peened surface and pristine surfaces are ~22.84µm and ~65.71µm, respectively. The higher R_a of the unpneed surface is noteworthy as it has a significantly lower R_a than that of the AWJ peened surface, prior to hot corrosion.
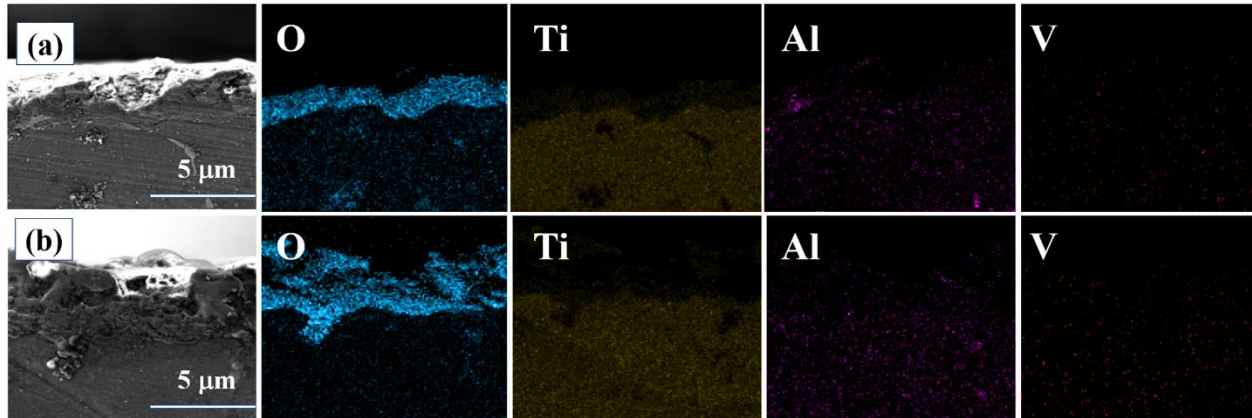
Fig.9. Cross sectional morphology of hot corroded morphologies (a) AWJ peened Ti-6Al-4V alloy, (b) Pristine Ti-6Al-4V alloy, with corresponding EDS maps after 80h of exposure.

To characterize the types of oxides on the two surfaces the XPS data obtained from them is analyzed. Figs. 10 and 11 shows the XPS scans of the pristine and AWJ peened surfaces of Ti-6Al-4V. The XPS peaks were fitted with a Gaussian distribution function in the CASAXPS software. On both surfaces, peaks corresponding to core levels of Ti 2p, O 1s, Al 2p and V 2p are observed. The Ti 2p core level in the XPS scans from both surfaces exhibit two peaks with binding energies of 457 eV and 463 eV that corresponds to Ti 2p3/2 and Ti 2p1/2, and a small shoulder corresponding to Ti 2p1/2 at a binding energy of 459.87 eV. These peaks confirm the Ti^{2+} and Ti^{3+} valence states of Ti in the oxide scale, respectively. Similarly, the O 1s core level samples shows two peaks at a binding energy of 528.5 eV, which corresponds to lattice oxygen associated with the Ti–O bond (TiO_2), and at 531.5 eV, which is associated with adsorbed oxygen. Al 2p also consist of two peaks of binding energy of 72.5 eV and 74 eV, corresponding to Al in the pure form and Al_2O_3, respectively. Interestingly, the V 2p spectrum from both surfaces are asymmetrically broadened. This indicates that the V 2p peak is not in a single valence state and curve fitting reveals the presence of three peaks at the binding energies of 515 eV, 516.1 eV and 517.2 eV. These energies correspond to V_2O_3, VO_2 and V_2O_5, respectively. Nevertheless, the VO_2 peak from both

surfaces is relatively prominent compared to the V_2O_5 and V_2O_5 peaks, which implies that the oxide has a higher proportion of the former. Although all the XPS peaks obtained from both surfaces are almost identical, their intensities and positions slightly vary. While the peak shifts are attributed to the differences in residual stress profiles of the two surfaces, the higher intensities of the peak from the pristine surface indicates that it is richer in oxide content. These results suggest that the oxide film on the surfaces contain TiO_2, Ti_2O_3, Al_2O_3, VO_2, V_2O_5 and V_2O_3.Overall, both AWJ peened and pristine surfaces gain mass, in the form of oxides, when covered with NaCl and exposed to 600 °C in atmosphere. While the extent and rate of oxide formation is higher in the pristine surface compared to that on the AWJ peened surface, their compositions are identical as both contain oxides of Ti, Al and V.

To further confirm the presence of the three oxides, TEM analysis of the hot corroded AWJP Ti–6Al–4V is performed. Fig. 12 displays the bright field TEM image and EDS maps of the oxide-metal interface in hot corroded AWJ peened Ti–6Al–4V. The presence of O in the top layer indicates that it is the oxide film, whereas the bottom portion is the unoxidized metal surface. The presence of Ti, Al and V in the top layer indicates that their oxides are present in it.
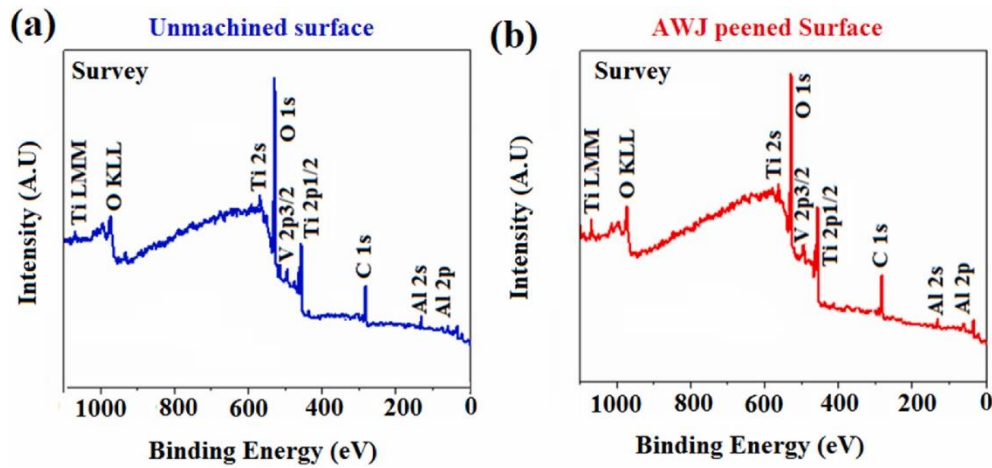
Fig.10. XPS spectrum of hot corroded samples- (a) AWJ peened sample, (b) pristine sample.
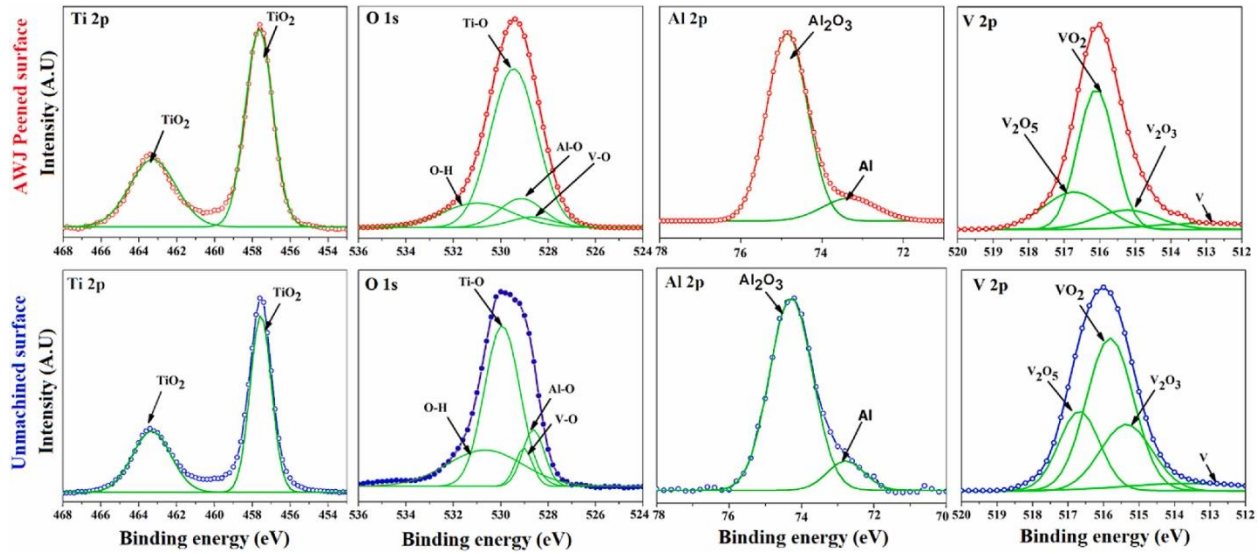

Fig.11 XPS passive film analysis of hot corroded samples- (a) AWJ peened sample, (b) pristine sample.
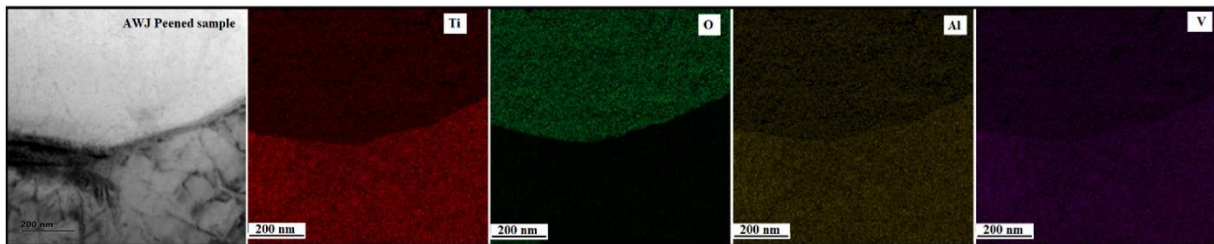

Fig. 12. Bright field TEM image of the oxide-metal interface in hot corroded AWJP Ti–6Al–4V and the corresponding EDS maps of Ti, O, Al and V.

4. Discussions

4.1. Effect of AWJ peening

During AWJ peening, the abrasive slurry bombards over a metallic surface or target, generating pressure pulses in the form of a shock envelope between the solid-liquid interface. After impact, within a few micro-seconds, the compression zone in the liquid breaks, initiating lateral outflows of the jets that impinge and create dilatational stress waves over the target [23-25]. The impact pressure is uniform over the surface, owing to the low impact angle of 30°, which prevents flaring of the slurry impact over the surface. The low impact angle and use of blunt Al_2O_3 balls in the AWJ process results in peening instead of material removal [24]. This causes plastic deformation and build-up of compressive residual stresses on surfaces as was seen in the AWJ peened Ti-6Al-4V surface (see Figs. 4 and Fig. 5). The magnitude and spacial extent up to which residual stresses develop depends on the duration for which the surface is subjected to AWJ peening. In some cases, the pressure waves generated can cause severe plastic deformation that can lead to formation of cracks and pockmarks on the surface. However, the absence of these features on the AWJ peened Ti-6Al-4V surface, shown Fig.3(b), indicates that the material has not undergone fracture. Nevertheless, the plastic deformation from the impact during AWJ peening will increase the dislocation density significantly and lead to the formation of sub-grains. The formation of subgrains and fragmentation of β-Ti lamellae in Fig. 6(b) is attributed to this effect. Moreover, undulations form on the surface which manifests as increased surface roughness [24], as was observed in Fig. S1.
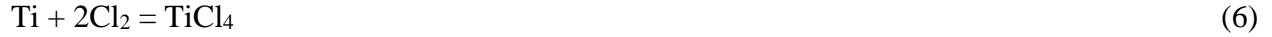
4.2. Mechanism of hot corrosion

Coating Ti-6Al-4V with NaCl and subjecting it to 600°C, leads to the diffusion of sodium and chloride ions into the alloy surface. The chloride ions and oxygen in the furnace oxidizes Ti and Al to form oxides and chlorine gas [13,29]. Some of these reactions are summarized as follows,

$$2NaCl + 2Al + 2O_2 \rightarrow 2NaAlO_2 + Cl_2 \qquad\qquad (1)$$

$$4NaCl + 2Ti + 3O_2 \rightarrow 2Na_2TiO_3 + 2Cl_2 \qquad\qquad (2)$$

In addition, Ti and Al react directly with oxygen to form TiO_2 and Al_2O_3 via the following reactions.

$$Ti + O_2 = TiO_2 \qquad\qquad \Delta G^o{}_{600°C} = \text{-930 kJ/mol} \quad (3)$$

$$4Al + 3O_2 = 2Al_2O_3 \qquad\qquad \Delta G^o{}_{600°C} = \text{-935 kJ/mol} \quad (4)$$

Where $\Delta G^o{}_{600°C}$ is the change in Gibbs free energy for each reaction. Although reaction (4), where Al_2O_3 forms, has a lower $\Delta G^o{}_{600°C}$ compared to reaction (3), Ti has a higher concentration in the alloy, which indicates its higher activity. Therefore, TiO_2 forms first, followed by Al_2O_3 and vanadium oxides (VO_2, V_2O_5, V_2O_3 and V_3O_5), which also have negative $\Delta G^o{}_{600°C}$ [9]. From prior studies, a sequence of events leading to the formation of the oxide scale during hot corrosion of Ti-6Al-4V is summarized as follows [17, 18]. A thin scale of TiO_2 forms first resulting in a Ti-poor, Al-rich zone at the interface between the oxide scale and alloy. The oxidation reaction progresses from the Al-rich zone as the Al diffuses through the loose TiO_2 scale and reacts with O_2 to form an intermittent Al_2O_3 scale. The TiO_2 scale becomes thicker as the oxidation reaction progresses and is accompanied by thin scales of V oxides and Al_2O_3. The thickness of V oxides and Al_2O_3 is low owing to their relatively lesser concentration in the alloy. With increasing time, Ti in the alloy diffuses outward through the oxide layers and deposits as an outer TiO_2 layer. Furthermore, in the presence of NaCl, it acts as a catalyst for oxychlorination thereby promoting hot corrosion. Note that Ti and oxides formed on the Ti-6Al-4V surface will also react with chloride ions that diffuse from the surface and produce volatile metal chlorides such $TiCl_2$, $TiCl_4$ and $AlCl_3$ [9,18,29] via the following reactions.

$$TiO_2 + 2Cl^- = TiCl_2 + 2O^{2-} \tag{5}$$

$$Ti + 2Cl_2 = TiCl_4 \tag{6}$$

$$Al_2O_3 + 6Cl^- = 2AlCl_3 + 3O^{2-} \tag{7}$$

The chlorides formed in reaction (5) and (6) can react further with oxygen to produce oxides, as described by the following reactions [18]:

$$TiCl_4 + O_2 = TiO_2 + 2Cl_2 \tag{8}$$

$$4AlCl_3 + 3O_2 = 2Al_2O_3 + 6Cl_2 \tag{9}$$

The Cl_2 produced reacts with Ti as described in reaction (6). As time progresses the thickness of the metal oxide layers increases on the Ti-6Al-4V surface. Note that the oxide films are less dense and have higher molar volume than the substrate. Therefore, owing to the lattice mismatch between the oxide layers and Ti-6Al-4V substrate, the increase in thickness of oxide layers causes coherency strains at the oxide/alloy interface [19]. Additionally, the metallic chlorides and Cl_2 formed from reactions (5), (6), (7), (8) and (9) escape by creating pores and cracks on the oxides. The combined effect of interface incoherence and pressure created by escaping gasses leads to delamination and spallation of the oxide, as was seen in the pristine Ti-6Al-4V surface (see Fig. 6(b)). A similar effect of elevated Cl levels on delamination of Ti-6Al-2Sn-4Zr-6Mo alloy/oxide interfaces was observed by Joseph et al [31].

Interestingly, the thickness of oxide films formed over the AWJ peened surface is lower than that on the pristine surface even though the composition of the oxide scales formed on them are similar. Moreover, hot corrosion rate, measured as K_p, for AWJ peened surface is less than 50% of that on pristine surfaces (see Fig. 8(b)). This is even more confounding, given that the former has higher

initial roughness (see Fig. S1), and hence more available sites for pitting corrosion [32], than the latter. We believe that the better corrosion resistance of the AWJ peened surface is the outcome of compressive residual stresses developing on it during peening. A schematic illustration of the mechanism for hot corrosion of pristine and AWJ peened surfaces is shown in Fig. 13. Note that corrosion initiates when chloride ions and oxygen diffuse into the surface and oxidize Ti and Al. Since the AWJ peened surface has residual compressive stresses, the diffusion rate of chloride ions and oxygen is slower than that on the pristine surfaces. Additionally, owing to rapid diffusion on the pristine surface, the hot corrosion reactions (5)-(9) also occur at a faster rate than that on the AWJ peened surfaces. Consequently, the greater volume of metallic chloride gasses and Cl_2 generated from these reactions leads to spallation and the formation of several pores on the oxide film surface. The rougher surfaces of the oxide film on pristine surfaces (see Fig. S4) are an outcome of the latter whereas the continuous delamination of the oxide layer manifests as the formation of loose oxide layers (see section 3.2).

To benchmark the effectiveness of AWJ peening in mitigating hot corrosion, it is important to also compare the hot corrosion behavior of surfaces prepared by other methods like ultrasonic shot peened (USSP), laser shock peening and hot isostatic pressing. Unfortunately, apart from one study on the effect of USSP on Ti-6Al-4V by Kumar et al. [19], the testing temperatures and salts used were different from those used in our study, which makes it difficult to make a direct comparison. Nevertheless, the corrosion rates of USSP and AWJ peened surfaces can be directly compared as hot corrosion tests were performed under identical conditions. It was observed that USSPed Ti-6Al-4V 600 °C after exposure to NaCl for 100 h, has a K_p of ~0.63 mg^2/cm^4/h, whereas that of the pristine surface is 4 times higher [9]. Considering that the K_p for AWJ peened surface is 2.5 lesser than that of the pristine surface, USSP appears to be slightly better in preventing hot corrosion of

the alloy. One possible reason for this is that USSP may have introduced compressive residual stresses deeper in the material. It is therefore likely that by increasing the peening exposure time, the same degree of hot corrosion resistance can be achieved in AWJ peened Ti-6Al-4V surfaces. One notable caveat in this comparison is that the absolute values of K_p on pristine surfaces in both studies are an order of magnitude different. This implies that performing tests under perfectly identical conditions is still a challenge and that further investigations comparing the hot corrosion rate of USSPed and AWJ peened Ti-6Al-4V need to be carefully standardized.

Before closing, it is worth mentioning that oxygen plays a critical role in the formation of Ti and Al oxide scales on the surface of Ti-6Al-4V. This is because reactions (1)-(4), which constitute the initial stages of scale formation, cannot occur in an oxygen free environment. For instance, Królikowska et.al [33], noted the absence of $NaAlO_2$ and Na_2TiO_3 in the scales of their hot corroded specimens when they conducted tests in salt solutions. Moreover, in such oxygen free conditions, such oxide scales also fail to form at temperature < 800 °C. This shows that the presence of oxygen enhances the reactivity of NaCl with Ti alloy as we observe the formation of $NaAlO_2$ and Na_2TiO_3 even at temperatures as low as < 800 °C [9,31].
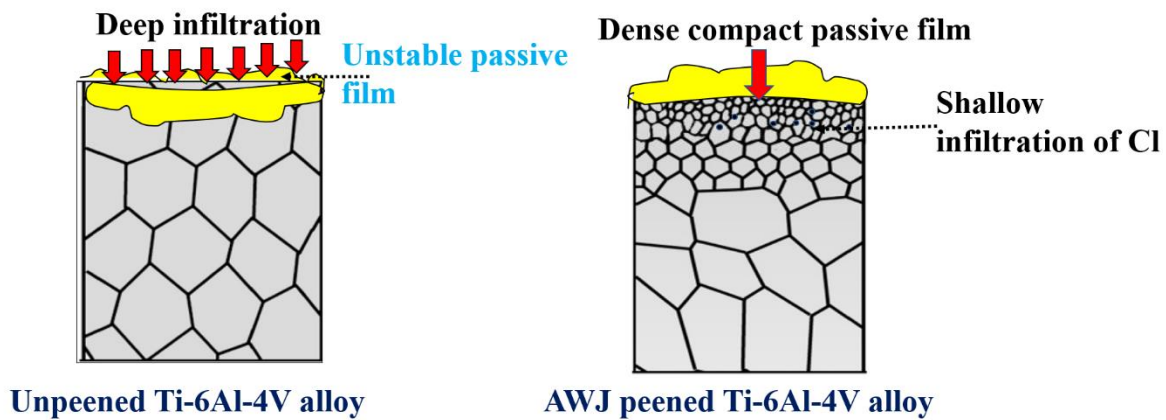
Fig.13. Schematic illustration on passive film formation on unpeened wrought alloy and AWJ peened Ti-6Al-4V surfaces.

From the results of this study, it becomes apparent that preventive measures against hot corrosion requires component isolation from oxygen, in addition to introducing compressive residual stresses on the surface. In future work, it is worth examining the extent to which AWJ peening process can improve the hot corrosion resistance of other engineering materials.

5. Conclusion

The effects of AWJ peening on NaCl induced hot corrosion behavior was studied for Ti6Al4V alloy. AWJ peening was first optimized with the intention of minimizing surface abrasion, however this results in grain refinement, surface roughening and introduction of compressive residual stresses on the surface. On coating both surfaces with NaCl and exposing them to 600 °C for 100 h, the AWJ peened surface exhibits 2.5 times better corrosion resistance than the pristine surface. Moreover, the oxide scale on the pristine surface is thicker and contains many pores. Composition analysis reveals that both surfaces have an oxide scale consisting of TiO_2, Al_2O_3, V_2O_3 and V_2O_5. Based on these observations, the operative chemical reactions were identified and it was determined that infiltration of chloride ions into the alloy surface initiates corrosion and also releases a large volume of chloride gasses. Conversely, the AWJ peened surface has a thinner and compact passive film. The lower mass gain of the AWJ peened surface could be attributed to compressive residual stresses on the surface, which retards the sub-surface diffusion of chloride ions. On comparing the hot corrosion resistance of AWJ peening with USSP it was observed that the latter was relatively more effective possibly due to a larger sub-surface layer with compressive

residual stresses. Nevertheless, AWJ peening has great potential in preventing hot corrosion resistance of Ti-6Al-4V alloys.

References

[1]   M. Rashid, R.L. Narayan, D.L. Zhang, W.Z. Han, A Comparative Study of Microstructures and Mechanical Behavior of Laser Metal Deposited and Electron Beam Melted Ti-6Al-4V, J. Mater. Eng. Perform. 31 (2022) 542–551. https://doi.org/10.1007/s11665-021-06197-y.

[2]   S. Huang, P. Kumar, W.Y. Yeong, R.L. Narayan, U. Ramamurty, Fracture behavior of laser powder bed fusion fabricated Ti41Nb via in-situ alloying, Acta Mater. 225 (2022) 117593. https://doi.org/10.1016/j.actamat.2021.117593.

[3]   L. Zhang, R.L. Narayan, H.M. Fu, U. Ramamurty, W.R. Li, Y.D. Li, H.F. Zhang, Tuning the microstructure and metastability of β-Ti for simultaneous enhancement of strength and ductility of Ti-based bulk metallic glass composites, Acta Mater. 168 (2019) 24–36. https://doi.org/10.1016/j.actamat.2019.02.002.

[4]   L. Tian, R.L. Narayan, K. Zhou, R. Babicheva, U. Ramamurty, Materials Science & Engineering A A real-time TEM study of the deformation mechanisms in β -Ti reinforced bulk metallic glass composites, Mater. Sci. Eng. A. 818 (2021) 141427. https://doi.org/10.1016/j.msea.2021.141427.

[5]   S. Huang, R.L. Narayan, J. Heang, K. Tan, S. Leong, W. Yee, Acta Materialia Resolving the porosity-unmelted inclusion dilemma during in-situ alloying of Ti34Nb via laser powder b e d fusion, Acta Mater. 204 (2021) 116522. https://doi.org/10.1016/j.actamat.2020.116522.

[6]   C.S. Ramachandran, V. Balasubramanian, P. V Ananthapadmanabhan, On the cyclic hot corrosion behaviour of atmospheric plasma sprayed Lanthanum Zirconate based coatings in contact with a mixture of sodium sulphate and vanadate salts: a comparison with the traditional Ysz duplex and NiCrAlY coated samples, Vacuum 97 (2013) 81–95, https://doi.org/10.1016/j. vacuum.2013.03.020.

[7]   M. Mohammadi, S. Javadpour, S.A.J. Jahromi, K. Shirvani, A. Kobayashi, Characterization and hot corrosion performance of LVPS and HVOF-CoNiCrAlYSi coatings, Vacuum 86 (2012) 1458–1464, https://doi.org/10.1016/j. vacuum.2012.02.030.

[8]   K. Yuan, R. Lin Peng, X.-H. Li, S. Johansson, Hot corrosion behavior of HVOF-sprayed CoNiCrAlYSi coatings in a sulphate environment, Vacuum 122 (2015) 47–53, https://doi.org/10.1016/j.vacuum.2015.09.015.

[9]   S. Kumar, K. Chattopadhyay, G.S. Mahobia, V. Singh, Hot corrosion behaviour of Ti – 6Al – 4V modi fi ed by ultrasonic shot peening, JMADE. 110 (2016) 196–206. https://doi.org/10.1016/j.matdes.2016.07.133.

[10]   H. Wu, P. Gong, S. Hu, L. Xiang, E. Wang, H. Xiao, Y. Wan, H. Ning, Z. Xie, Hot corrosion damage mechanism of Ti6Al4V alloy in marine environment, Vacuum. 191 (2021) 110350. https://doi.org/10.1016/j.vacuum.2021.110350.

[11]   M. Anuwar, R. Jayaganthan, V.K. Tewari, N. Arivazhagan, A study on the hot corrosion behavior of Ti – 6Al – 4V alloy, 61 (2007) 1483–1488. https://doi.org/10.1016/j.matlet.2006.07.058.

[12]   Q. Xu, W. Li, Y. Yin, J. Zhou, H. Nan, Materials Science & Engineering A Effect of hot isostatic pressing on the cast Ti6Al4V alloy with shrinkage cavities inside : Healing behavior ,

microstructure evolution and tensile property, Mater. Sci. Eng. A. 832 (2022) 142496. https://doi.org/10.1016/j.msea.2021.142496.

[13]   H. Lu, Z. Wang, J. Cai, X. Xu, K. Luo, L. Wu, J. Lu, Effects of laser shock peening on the hot corrosion behaviour of the selective laser melted Ti6Al4V titanium alloy, Corros. Sci. 188 (2021) 109558. https://doi.org/10.1016/j.corsci.2021.109558.

[14]   W. Guo, R. Sun, B. Song, Y. Zhu, F. Li, Z. Che, B. Li, C. Guo, Surface & Coatings Technology Laser shock peening of laser additive manufactured Ti6Al4V titanium alloy, 349 (2018) 503–510. https://doi.org/10.1016/j.surfcoat.2018.06.020.

[15]   M. Palanivel, R. Bhardwaj, L. Edalacheruvu, R. Nagumothu, Materials Today : Proceedings Development of corrosion-resistant and hydrophobic coating on commercially pure titanium, Mater. Today Proc. 46 (2021) 1017–1021. https://doi.org/10.1016/j.matpr.2021.01.215.

[16]   S. Slawik, S. Bernarding, F. Lasagni, C. Navarro, F. Boby, S. Migot-choux, J. Domínguez, F. Mücklich, A. Peri, Materials Characterization Microstructural analysis of selective laser melted Ti6Al4V modified by laser peening and shot peening for enhanced fatigue characteristics, 173 (2021). https://doi.org/10.1016/j.matchar.2021.110935.

[17]   P. Vlcak, J. Fojt, J. Koller, J. Drahokoupil, V. Smola, Results in Physics Surface pre-treatments of Ti-Nb-Zr-Ta beta titanium alloy : The effect of chemical , electrochemical and ion sputter etching on morphology , residual stress , corrosion stability and the MG-63 cell response, Results Phys. 28 (2021) 104613. https://doi.org/10.1016/j.rinp.2021.104613.

[18]   C. Ciszak, I. Popa, J. Brossard, D. Monceau, S. Chevalier, NaCl induced corrosion of Ti-6Al-4V alloy at high temperature, Eval. Program Plann. 110 (2016) 91–104. https://doi.org/10.1016/j.corsci.2016.04.016.

[19]   P. Kumar, G.S. Mahobia, S. Mandal, V. Singh, K. Chattopadhyay, Enhanced corrosion resistance of the surface modified Ti-13Nb-13Zr alloy by ultrasonic shot peening, Corros. Sci. 189 (2021) 109597. https://doi.org/10.1016/j.corsci.2021.109597.

[20]   N. Tapoglou, R.M. Saoubi, T. Childerhouse, E. Hern, L. Franca, W. Leahy, M. Jackson, The influence of finish machining depth and hot isostatic pressing on defect distribution and fatigue behaviour of selective electron beam melted, 147 (2021) 1–11. https://doi.org/10.1016/j.ijfatigue.2021.106169.

[21]   E. Maleki, S. Bagherifard, M. Bandini, M. Guagliano, Surface post-treatments for metal additive manufacturing : Progress , challenges , and opportunities, Addit. Manuf. 37 (2021) 101619. https://doi.org/10.1016/j.addma.2020.101619.

[22]   Y. Natarajan, P.K. Murugesan, M. Mohan, S. Ahmed, L. Ali, Abrasive Water Jet Machining process : A state of art of review, J. Manuf. Process. 49 (2020) 271–322. https://doi.org/10.1016/j.jmapro.2019.11.030.

[23]   Z. Liao, I. Sanchez, D. Xu, D. Axinte, G. Augustinavicius, Dual-processing by abrasive waterjet machining — A method for machining and surface modi fi cation of nickel-based superalloy, J. Mater. Process. Tech. 285 (2020) 116768. https://doi.org/10.1016/j.jmatprotec.2020.116768.

[24]   M. Srivastava, S. Hloch, N. Gubeljak, M. Milkovic, Surface integrity and residual stress analysis of pulsed water jet peened stainless steel surfaces, Measurement. 143 (2019) 81–92. https://doi.org/10.1016/j.measurement.2019.04.082.

[25]   A.K. Amar, P. Tandon, CIRP Journal of Manufacturing Science and Technology Investigation of gelatin enabled abrasive water slurry jet machining, CIRP J. Manuf. Sci. Technol. 33 (2021) 1–14. https://doi.org/10.1016/j.cirpj.2021.02.005.

[26]   G. Greczynski, L. Hultman, Reliable determination of chemical state in x-ray photoelectron spectroscopy based on sample-work-function referencing to adventitious carbon: resolving the myth of apparent constant binding energy of the C 1s peak, Appl. Surf. Sci. 451 (2018) 99–103.

[27]   G. Greczynski, L. Hultman, X-ray photoelectron spectroscopy: towards reliable binding energy referencing, Prog. Mater. Sci. 107 (2020), 100591, https://doi.org/10.1016/j.pmatsci.2019.

[28]   G. Greczynski, L. Hultman, A step-by-step guide to perform x-ray photoelectron spectroscopy, J. Appl. Phys. 132 (1) (2022), 011101, https://doi.org/10.1063/5.0123879.

[29]   Y. Zhang, Z. Liu, X. Zhang, Q. Wang, Q. Wang, H. Wang, W. Jiang, S. Liu, C. Liu, N. Wang, Y. Cui, The formation mechanism of (001) preferred orientation for anatase TiO2 film prepared by DC pulsed magnetron sputtering, Vacuum 190 (2021), 110287.

[30]   S. Zhang, W. Guo, N. Liu, C. Xia, H. Wang, C. Liang, In situ preparation of MAO/ TiO2 composite coating on WE43 alloy for anti-corrosion protection, Vacuum 197 (2022), 110835.

[31]   S. Joseph, T.C. Lindley, D. Dye, E.A. Saunders, The mechanisms of hot salt stress corrosion cracking in titanium alloy, Corros. Sci. 134 (2018) 169–178. https://doi.org/10.1016/j.corsci.2018.02.025.

[32]   L. Sun, Q. Fu, J. Sun, Effect of SiO 2 barrier scale prepared by pre-oxidation on hot corrosion behavior of MoSi 2 -based coating on Nb alloy, Corros. Sci. 176 (2020) 109051. https://doi.org/10.1016/j.corsci.2020.109051.

[33] M. Mitoraj-królikowska, E. Godlewska, Hot corrosion behaviour of (γ + α2) -Ti-46Al-8Nb (at.%) and α-Ti-6Al-1Mn (at.%) alloys, Eval. Program Plann. 115 (2017) 18–29. https://doi.org/10.1016/j.corsci.2016.11.006.